Watching Death in the Gerbil Cochlea Using Optical Coherence Tomography

Nam Hyun Cho[1,2], Haobing Wang[1,2], and Sunil Puria[1,2,3,*]

[1]Department of Otolaryngology-Head and Neck Surgery, Harvard Medical School, Boston, MA, 02114, USA
[2]Eaton-Peabody Laboratories, Massachusetts Eye and Ear, Boston, MA, 02114, USA
[3]Speech and Hearing & Bioscience and Technology Program, Harvard University, Cambridge, MA, 02138, USA

*Corresponding Author: Email: Sunil_Puria@meei.harvard.edu

Abstract

Because it is difficult to directly observe the morphology of the living cochlea, our ability to infer the mechanical functioning of the living ear has been limited. Nearly all of our knowledge about cochlear morphology comes from postmortem tissue that was fixed and processed using procedures that possibly distort the structures and fluid spaces of the organ of Corti. In this study, optical coherence tomography was employed to obtain in vivo and postmortem micron-scale volumetric images of the high-frequency hook region of the gerbil cochlea through the round-window membrane. The anatomical structures and fluid spaces of the organ of Corti were segmented and quantified in vivo and over a 90-minute postmortem period. The results show that some aspects of the organ of Corti are significantly altered over the course of death, such as the volumes of the fluid spaces, whereas the dimensions of other features change very little. We postulate that the fluid space of the outer tunnel and its surrounding tectal cells form a resonant structure that can affect the motion of the reticular lamina and thereby have a profound effect on outer-hair-cell transduction and thus cochlear amplification. In addition, the in vivo fluid pressure of the inner spiral sulcus is postulated to effectively inflate the connected sub-tectorial gap between the tectorial membrane and the reticular lamina. This gap height decreases after death, which is hypothesized to reduce and disrupt hair-cell transduction

I. Introduction

A touchstone of biological research is the notion that structure determines function. In the auditory system, hearing function is closely associated with the intricate structure of the organ of Corti (OoC), the sensory epithelium within the spiral-shaped, fluid-filled cochlea of the inner ear. The OoC itself is attached to the basilar membrane (BM), which partitions the cochlear fluid space as it runs along the length of the spiral from the high-frequency basal hook region (Fig. 1a, b) to the low-frequency apical end of the cochlea.

While there has been rapid progress in the use of optical coherence tomography (OCT) for in vivo vibrometry measurements of cochlear function, little attention has been paid to the morphology of the OoC in the living cochlea. Nearly all of our knowledge about OoC cellular and extracellular structure comes from histologically processed, postmortem (PM) cochleae that have been decalcified, sliced, stained, and imaged with light or electron microscopy (Lim and Anniko, 1985; O'Malley et al., 2009; Plassmann et al., 1987). Alternate approaches include hemicochlea preparations and confocal microscopy using whole-mount preparations, but they also use PM tissue (Edge et al., 1998; Hardie et al., 2004). Although these are standard methods, their shortcomings include an uncertain relationship to the living anatomy and unknown preparation-related distortions of the fluid spaces and OoC structures. These unknowns have limited our ability to deduce function from anatomy, particularly in the high-frequency basal end of the cochlea that is partially important for sound localization.

The OoC fluid space is defined to contain the following: (1) the inner spiral sulcus (ISS), which is connected to the sub-tectorial fluid space; and (2) the cortilymph space consisting of the tunnel of Corti (ToC), the space of Nuel (SN), and the fluid space around the outer hair cells (OHCs) and outer tunnel (OT; Fig. 1c). In the middle turn of the gerbil cochlea, electrical stimulation of the OHCs has produced fluid waves in the ToC (Karavitaki and Mountain, 2007). Thus, knowledge of the OoC fluid spaces and surrounding structures is important for a full understanding of cochlear amplification (Zagadou et al., 2020). However, these fluid spaces are typically absent in histological images of the high-frequency hook region. As we will show, these absences are likely artifacts due to tissue processing. While many studies have focused on the OoC structures (Hu et al., 1999; Plassmann et al., 1987; Richter et al., 2000; Souter et al., 1995; Spicer et al., 2003), less attention has been paid to the OoC fluid spaces, and particularly the ISS and OT, which brings into question our current understanding of the structure–function relationships in the cochlea at high frequencies. To characterize the in vivo OoC structures and fluid spaces, anatomical methods that work in living animals are needed.

OCT is an optical imaging modality with micron-scale axial and lateral resolutions that enables non-invasive and non-destructive imaging of 2D cross sections and 3D volumes of unlabeled biological tissue using backscattered near-infrared broadband light source (Huang et al., 1991). It is used extensively in a variety of biomedical fields including ophthalmology and otolaryngology, and has additional applications for measuring vibration. OCT has been used to visualize morphological changes in the cochleae of blast- and noise-exposed mice (Kim et al., 2018; Liu et al., 2017), and to visualize changes to the vestibular system in guinea pigs caused by the surgical induction of endolymphatic hydrops (Cho et al., 2015). Micro-OCT (µOCT) technology has been used to image guinea pig temporal bones with sub-micron-level axial and lateral resolutions, allowing visualization of the cochlear microanatomy at a cellular level (Iyer et al., 2016). While the resolutions of µOCT images are the highest yet achieved for OCT imaging, these measurements were from ex vivo cochleae that were chemically fixed.
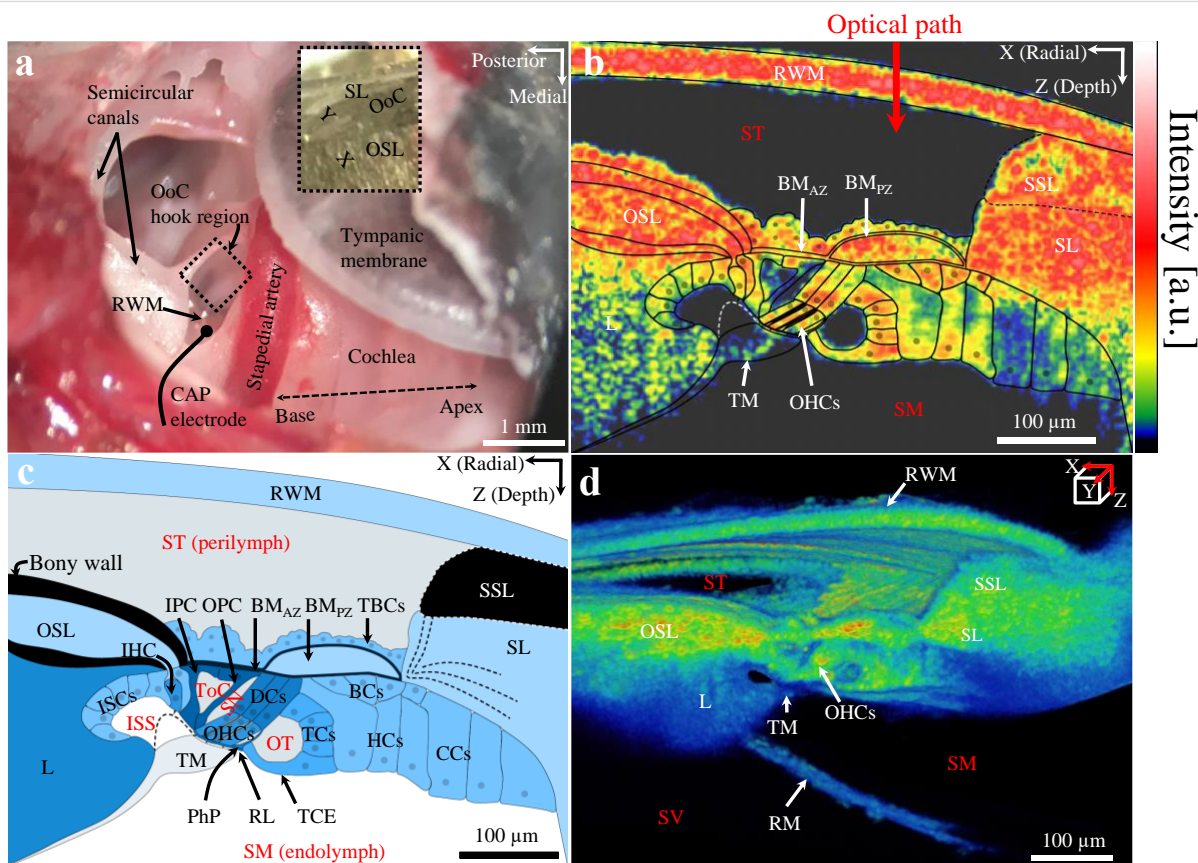
Fig. 1. The anatomy of the gerbil ear, as depicted by multiple modalities. **a:** A photograph of the surgically opened right middle ear shows the region of the round-window membrane (RWM; black dotted square), through which the organ of Corti (OoC) in the "hook region" of the cochlea (inset image) can be imaged using optical coherence tomography (OCT). The inset image, the X (radial) and Y (longitudinal) axes indicate the OCT scanning directions for 2D cross-section and 3D volume measurements, based on left-hand coordinates, with the Z (depth) direction pointing into the page. An electrode used for compound action potential (CAP) recordings was typically placed in the niche near the RWM (see Fig. SI-1 for CAP results). Animal #188R. **b:** A 2D cross-sectional OCT image overlaid with a line drawing of the cells and fluid spaces inferred from the image. The inner boundary of the tectorial membrane (TM) was not entirely visible in the OCT image, so a white dashed outline has been added to show its hypothesized full extent, in which a portion lies just above the IHC stereocilia bundle. (Additional abbreviations found in panels **b–d** are defined further below.) **c:** A labeled drawing of a representative OoC as seen through the RWM, based on the 2D OCT image in **b**. Note that different shades of blue indicate the relative stiffness of different structures, with lighter shades indicating more compliant materials. Cortilymph-filled spaces include the tunnel of Corti (ToC), space of Nuel (SN), outer tunnel (OT), and the spaces between the outer hair cells (OHCs; not shown). The continuation of the BM collagen fibers in the SL region are not entirely visible in this OCT image but are faintly visible in **d**. Note that the dashed lines in SL region have been added to represent these (Agrawal et al., 2018). **d:** A stack of 2D OCT-imaged cross-sections, ranging from ~0.1 to 1.1 mm from the basal end of the cochlea, forms a 3D volumetric representation of the OoC (Movie SI-1 is an animated scan of the image stack). **b-d** Right hand coordinate system. Animal #191. **Other abbreviations:** BCs: Boettcher cells; BM_{AZ} and BM_{PZ}: arcuate zone and pectinate zone of the basilar membrane, respectively; CCs: Claudius cells; DCs: Deiters' cells; HCs: Hensen's cells; IHC: inner hair cell; IPC and OPC: inner and outer pillar cell, respectively; ISCs: inner-sulcus cells; L: limbus; OSL: osseous (primary) spiral lamina; PhP: phalangeal process; RL: reticular lamina; RM: Reissner's membrane; SL: spiral ligament; SSL: (osseous) secondary spiral lamina; TBCs: tympanic border cells; TCs: tectal cells; TCE: tectal-cell extension; ST: scala tympani; SM: scala media; SV: scala vestibuli; and ISS: inner spiral sulcus; a.u.: arbitrary units.

46

47   In this study, we used commercial OCT hardware and custom-built software to collect in vivo
48   2D images of the gerbil OoC fluid spaces and surrounding structures in the basal-turn hook region.
49   The images were made through the intact round-window membrane (RWM; Fig. 1a, b), with axial
50   (in water) and lateral resolutions of ~1.4 and ~1.95 µm, respectively. In addition, each 3D-volume
51   scans having a depth of about 0.3 mm were obtained at multiple focal depths and then concatenated
52   to obtain about a 1-1.2 mm volume depth (Cho et al., 2018) (Fig. 1d). We obtained in vivo scans
53   over the course of 1 hour, and postmortem scans up to 90 min after death. This procedure allowed
54   us to image the OoC structures while the animal was alive, and to then observe changes in the
55   dimensions and orientations of the OoC structures and fluid spaces during and after the dying
56   process.
57   The fluid volumes of the ISS, ToC, SN, and OT, as well as the scala tympani (ST) region
58   between the RWM and BM, were segmented for analysis. To directly compare the OCT-based
59   morphometry against morphometry obtained using histological methods, we processed a subset of
60   ears using an aldehyde fixation followed by celloidin embedding and serial sectioning, an approach
61   reported to best preserve the delicate architecture of the inner ear epithelia (O'Malley et al., 2009).
62   We show that many dimensions of the OoC structures, fluid spaces, and cochlear ducts undergo
63   profound changes during the process of death, while others stay constant. Based on these
64   morphological observations, we propose new hypotheses concerning the role of the mechanics of
65   the OT fluid space on OHC transduction, and the effects of the ISS fluid space and sub-tectorial
66   gap on inner hair cell (IHC) and OHC transduction.
67

II. Results

69   We used 3 female and 2 male gerbils for the in vivo studies (N=5), with a subset of these (N=3)
70   also used for the postmortem studies. For each gerbil, in vivo 2D cross-sectional images (e.g., Fig.
71   1b) were acquired at ~5-min intervals over a 60-min period before the time of death. For three of
72   the gerbils, 2D cross-sectional images continued to be acquired over a 90-min PM period. Using a
73   consistent angular approach, 3D-volume scans (e.g., Fig. 1d, Movie SI-1) were acquired in vivo at
74   the beginning of the experiment and 60 min later, just before death, and at 10-, 30-, 60-, and 90-
75   min after death.
76   Figure 2 shows representative 2D images at selected time points of the living (top row), and
77   PM (rows 2 and 3) cochlea. The in vivo OoC structures and fluid spaces remained stable across
78   the 60-min interval. In the living cochlea, the RWM and Reissner's membrane (RM) were curved
79   and bulged outward away from the OoC. A time-lapse movie from the same ear (Movie SI-2)
80   shows major changes occurring in the cochlear anatomy after death. The middle row of Figure 2
81   shows that both the RWM and RM have started to recede toward the OoC as early as 10-min PM.
82   By 60-min PM, the RWM and RM have changed their directions of curvature, indicating decreased
83   volumes of the ST and scala media (SM). This is consistent with PM decreases in both the ST
84   pressure and the pressure difference between the SM and scala vestibuli (SV). Dimensions of rigid
85   structures such as the outer pillar cells (OPCs) that separate the ToC from the SN (Fig. 1c, Fig. 2
86   top row) generally remain stable.
87   Figure 2 qualitatively shows that the OoC structures and fluid spaces changed with death, and
88   that those changes continued to occur up to at least 90-min PM. At 30-min PM, the fluid spaces
89   for the ISS, ToC, SN, and OT appear similar to those at 10-min PM, so the 10-min PM results are
90   not shown in subsequent figures. By 30-min PM, there is a decreased ISS space, an increased OT

91   space, and a swelling of the OoC structure. By 90-min PM the OoC has swelled further (bottom
92   row).

93
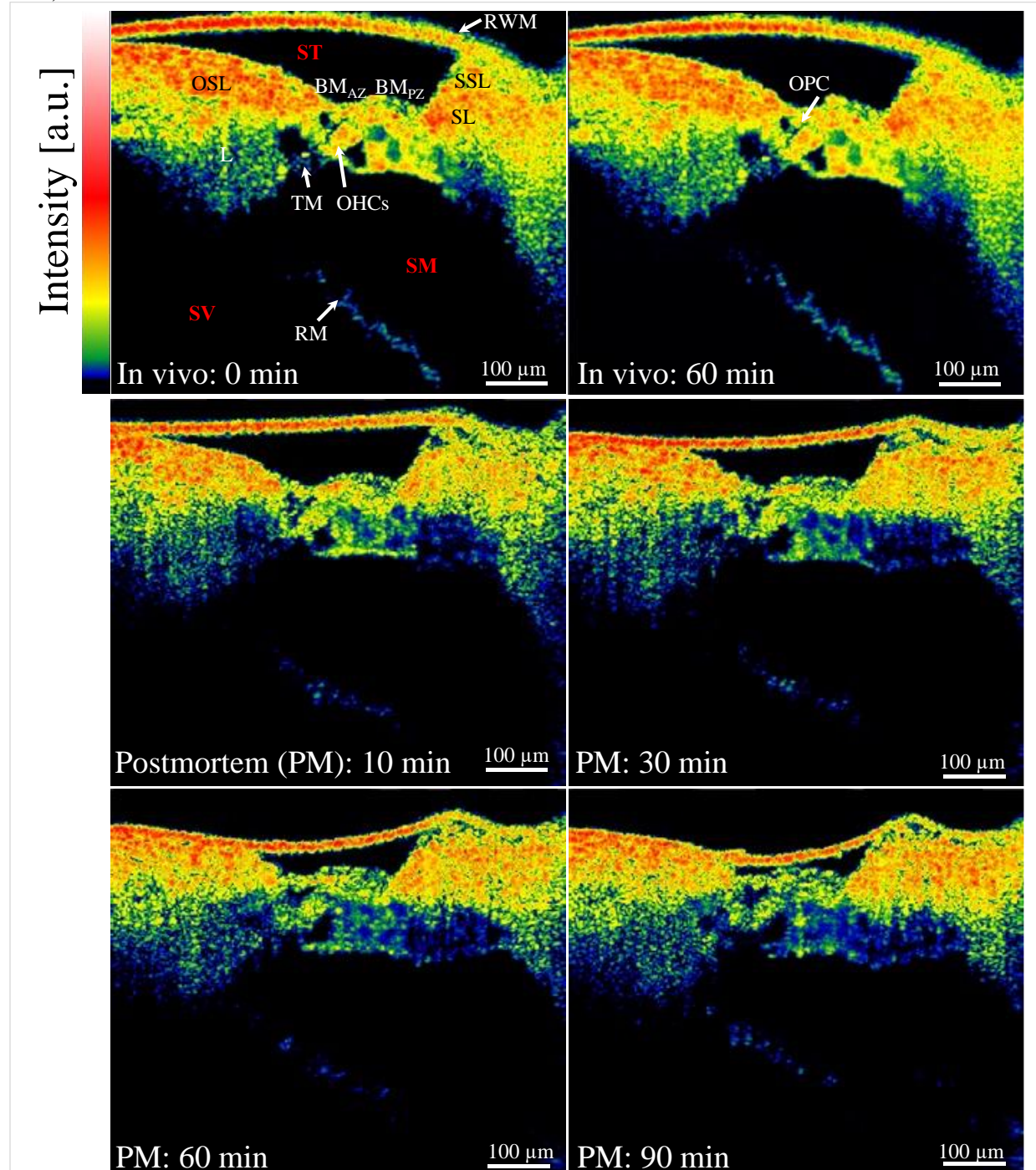
Fig. 2. OCT-based cross-sectional OoC images at two in vivo times 60-min apart (top row) and four postmortem (PM) times, at 10, 30, 60, and 90 min after death (rows 2 and 3). The similarities between the in vivo images indicate the stability of the living preparation. The sequence of PM images reveals the progression of changes to the cochlear morphology after death. The full set of cross-sectional images of the PM state, acquired at 5-minute increments, can be viewed as a time-lapse sequence (Movie SI-2). See the caption of Fig. 1 for a list of abbreviations. Animal #269.

Quantitative assessment of OoC structural changes from in vivo to postmortem

Figure 3a shows a 2D cross-sectional OCT image illustrating the gross dimensions of the OoC important for cochlear mechanics. To quantify the effects of death on the OoC structure and volume, the OoC width (OoC_W) and height (OoC_H) were measured for the in vivo and PM states and then compared (see SI-3, 4 for methods).

In the image, OoC_W is bounded by the osseous spiral lamina (OSL) to the left and the spiral ligament (SL) to the right (see also Fig. SI-2). OoC_H is bounded by the BM at the top and a combination of the reticular lamina (RL), tectal cells, and Hensen's cells at the bottom (see also Fig. SI-2b). The volume of the OoC cellular elements were calculated by subtracting the area of the fluid spaces (see Fig. 5) and integrating the remaining area along the longitudinal dimension. In the region evaluated, the volume per unit length of the structural components of the OoC increased by about 25% by 90-min PM (Fig. 3b). This increase in volume is likely due to swelling of the OoC cells.
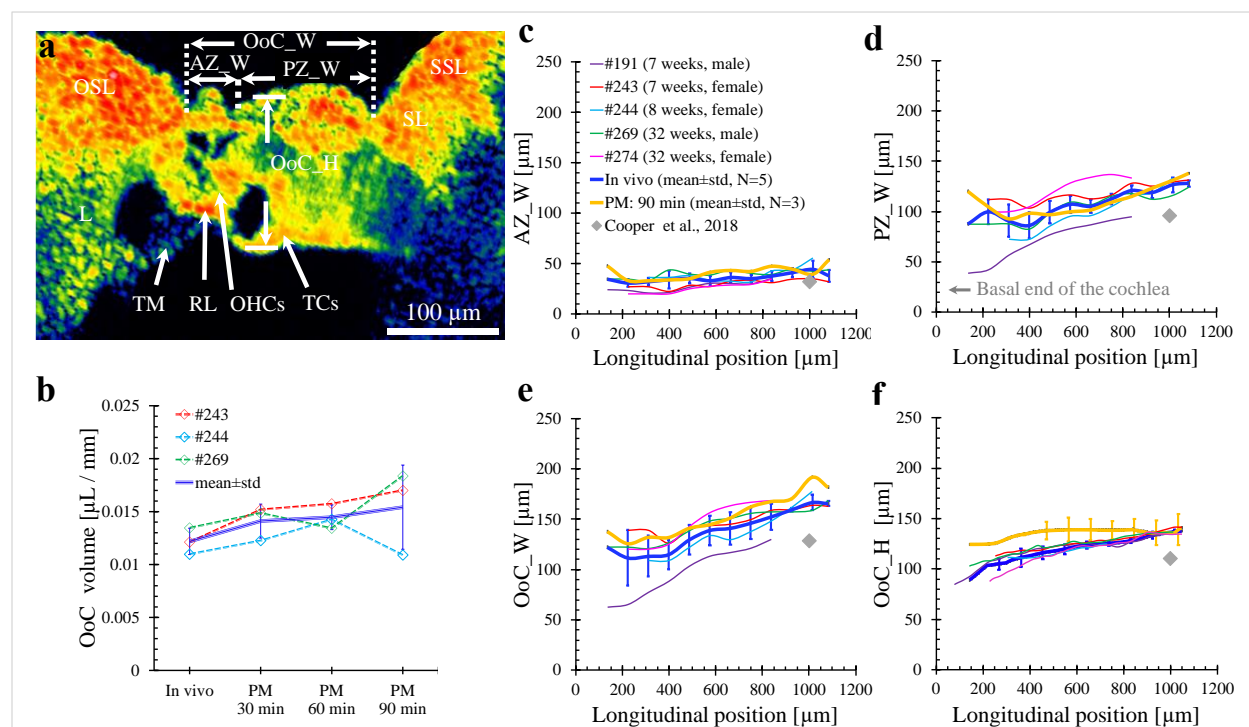

Fig. 3. OoC volume and dimensions across in vivo and PM times, and OoC in vivo linear dimensions versus longitudinal position in the cochlear hook region. **a:** This 2D cross-sectional image identifies the BM_{AZ} width (AZ_W) between the OSL ridge and the base of the first row of DCs, the BM_{PZ} width (PZ_W) between the base of the first row of DCs and the SL ridge, and the total OoC width (OoC_W) between the OSL and SL ridges, which is equivalent to the sum of AZ_W and PZ_W. The overall OoC height (OoC_H) is defined as the distance between the BM and the TCs or TCE (see Figs. SI-2 and 3 for segmentation details). Animal #243. **b:** Changes in the OoC volume per unit length (μL/mm) over time, from in vivo to 90-min PM for 3 specimens, along with the mean and standard deviation (std). **c–f:** The AZ_W, PZ_W, OoC_W, and OoC_H dimensions are plotted in respective panels as functions of longitudinal position (in μm) from the basal end of the cochlea. The mean±std error bars for the in vivo measurements (N=5) are shown as blue lines, and those for the 90-min-PM measurements (N=3) are shown as yellow lines. Individual in vivo cases (thin colored lines) are also shown, with the ID, age, and gender of each animal reported in panel **c**. In **c–f**, the gray diamonds are comparison measurements from in vivo OCT images reported by Cooper et al. (2018) for a location about 1 mm (~40 kHz region) from the basal end of the gerbil cochlea.

7

109   The width (AZ_W) and collagen-fiber content of the arcuate zone of the BM (BM$_{AZ}$) are
110   thought to play a dominant role in the place–frequency tonotopic map of the gerbil cochlea
111   (Kapuria et al., 2017). Thus, the total width of the BM (OoC_W) has been divided into AZ_W,
112   bounded by the OSL and the junction of the outer pillar cell and first row base of the Deiters' cells,
113   and PZ_W, the width of the pectinate zone of the BM (BM$_{PZ}$), which is bounded by the first row
114   base of Deiters' cells and the SL, as defined previously (see Fig. SI-2a, b, d) (Plassmann et al.,
115   1987; Richter et al., 2000). OoC_W is equivalent to the sum of AZ_W and PZ_W.
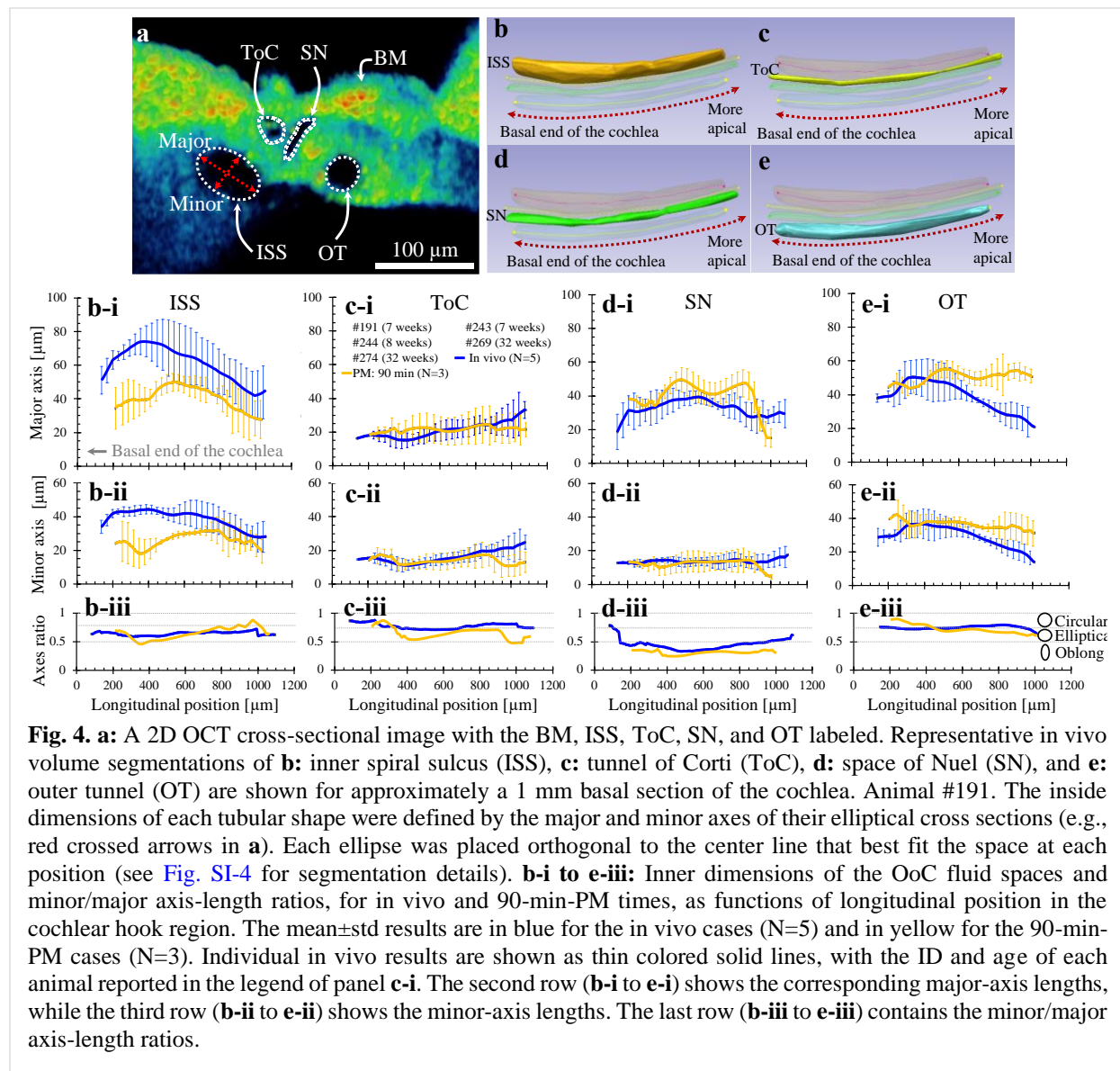116   Figure 3c–f contains plots of AZ_W, PZ_W, OoC_W, and OoC_H as functions of distance
117   from the basal end of the cochlea toward apex in the hook region over the ~0.1–1.1-mm range.
118   The starting position relative to the basal end of the cochlea was slightly different for each OCT
119   scan (see SI-5 for alignment information). The individual in vivo results are shown (thin colored
120   lines; N=5), along with their mean±standard deviation (std; thick blue lines and error bars), as well
121   as the mean±std (N=3) for the 90-min PM case (thick yellow lines and error bars). OoC_W and
122   OoC_H are slightly larger for the PM state than for the in vivo state. Generally, the dimensions of
123   the OoC increase from the base towards the apex (Fig. 3c–f), which is consistent with the
124   decreasing characteristic frequency in the apical direction that is a key feature of the mammalian
125   cochlea (Peterson and Bogert, 1950; Von Békésy, 1960). Despite the increases in all of these
126   dimensions as one moves apically, the AZ_W/OoC_W ratio maintains an approximately constant
127   value of around 0.25 (not shown). As a comparison, we estimated OoC dimensions based on an in
128   vivo OCT image near the 1-mm location, from Fig. 1c of Cooper et al. (Cooper et al., 2018). These
129   dimensions (gray diamonds in Fig. 3) are typically lower than the averages we found, by about
130   25%. Our measurements in animal #191 (purple lines), which was the youngest and one of the
131   lower weight animals studied (7 weeks, 72 g), are also lower than our average. The Cooper et al.
132   animal was about 12 weeks and 56 g. Thus, the differences between our results and those of Cooper
133   et al. could be due to lower animal weights, and/or perhaps different OCT-beam angles. The infant
134   and adult and thus age and weight-related OoC dimension differences are known in the human
135   (Meenderink et al., 2019).
136
137   **OoC fluid-space changes from in vivo to 90-minutes postmortem**
138   Figure 4 reports the major and minor axes of the OoC fluid subspaces as functions of cochlear
139   location. These subspaces were roughly elliptical in cross section (Fig. 4a). Segmentations of the
140   ISS, ToC, SN, and OT fluid spaces for a representative ear are presented in Figure 4b–e. Figure 4
141   shows the individual in vivo results (thin colored lines), the corresponding mean±std (N=5, thick
142   blue lines and error bars), and the mean±std for the 90-min PM results (N=3, thick yellow lines
143   and error bars), for the lengths of the major (row i) and minor (row ii) axes. Additionally, the
144   minor/major axis-length ratios are shown for the in vivo (blue lines) and 90-min PM (yellow lines)
145   means (row iii).
146   The ISS fluid space is bounded by the tectorial membrane (TM), limbus (L), and inner-sulcus
147   cells (ISCs), with a narrow opening for the sub-tectorial space (Fig. 1c), generally had the largest
148   in vivo dimensions (Fig. 4).
149   The average length of the ISS major axis for the in vivo case (Fig. 4b–i) generally increased
150   and then decreased reaching a maximum of about 74 µm. At 90-min PM, the average length of the
151   ISS major axis was smaller. Unlike the major axis, the ISS minor axis for the in vivo case (Fig.
152   4b–ii) exhibited a flatter longitudinal profile on average, with a value of about 44 µm in the 200–
153   600-µm range. At 90-min PM, the average length of the ISS minor axis was smaller.

8

Fig. 4. a: A 2D OCT cross-sectional image with the BM, ISS, ToC, SN, and OT labeled. Representative in vivo volume segmentations of **b:** inner spiral sulcus (ISS), **c:** tunnel of Corti (ToC), **d:** space of Nuel (SN), and **e:** outer tunnel (OT) are shown for approximately a 1 mm basal section of the cochlea. Animal #191. The inside dimensions of each tubular shape were defined by the major and minor axes of their elliptical cross sections (e.g., red crossed arrows in **a**). Each ellipse was placed orthogonal to the center line that best fit the space at each position (see Fig. SI-4 for segmentation details). **b-i to e-iii:** Inner dimensions of the OoC fluid spaces and minor/major axis-length ratios, for in vivo and 90-min-PM times, as functions of longitudinal position in the cochlear hook region. The mean±std results are in blue for the in vivo cases (N=5) and in yellow for the 90-min-PM cases (N=3). Individual in vivo results are shown as thin colored solid lines, with the ID and age of each animal reported in the legend of panel **c-i**. The second row (**b-i** to **e-i**) shows the corresponding major-axis lengths, while the third row (**b-ii** to **e-ii**) shows the minor-axis lengths. The last row (**b-iii** to **e-iii**) contains the minor/major axis-length ratios.
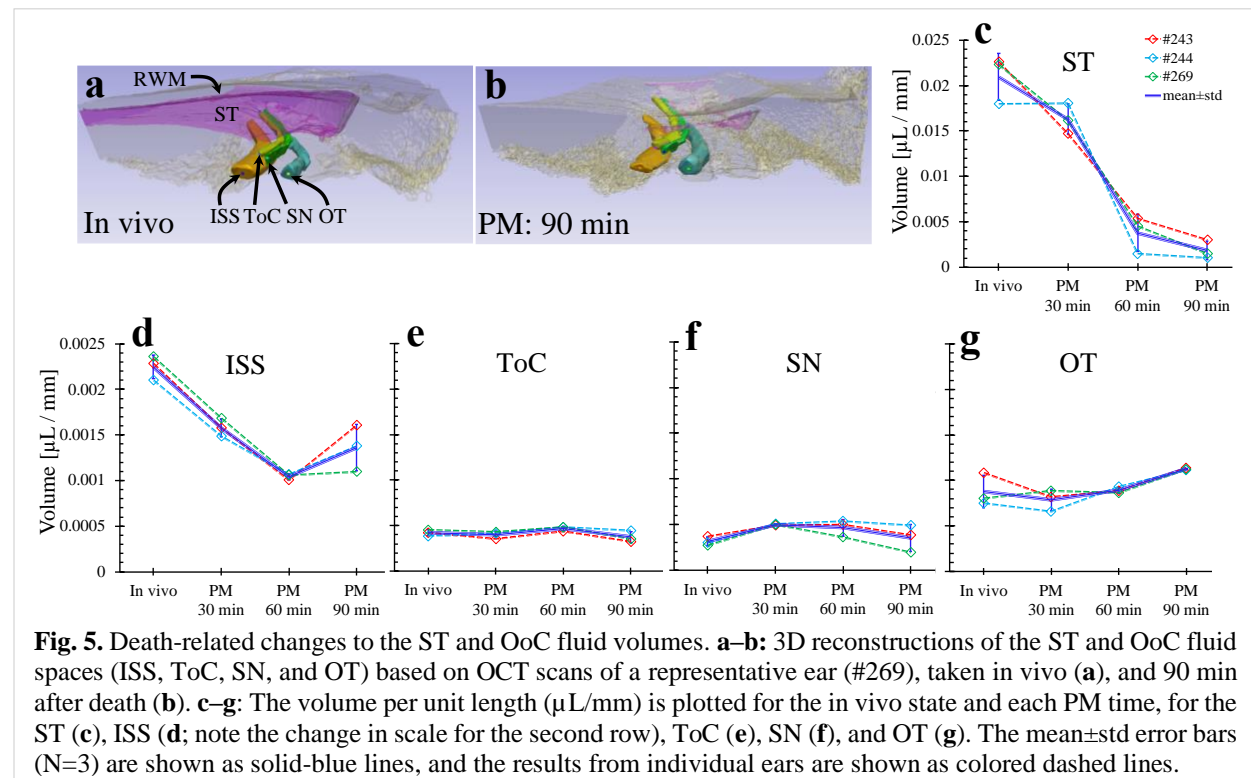
154
155   In general, the ISS major axis (Fig. 4b-i) showed a similar longitudinal profile between the in
156 vivo and 90-min PM cases, but with the in vivo case scaled higher.
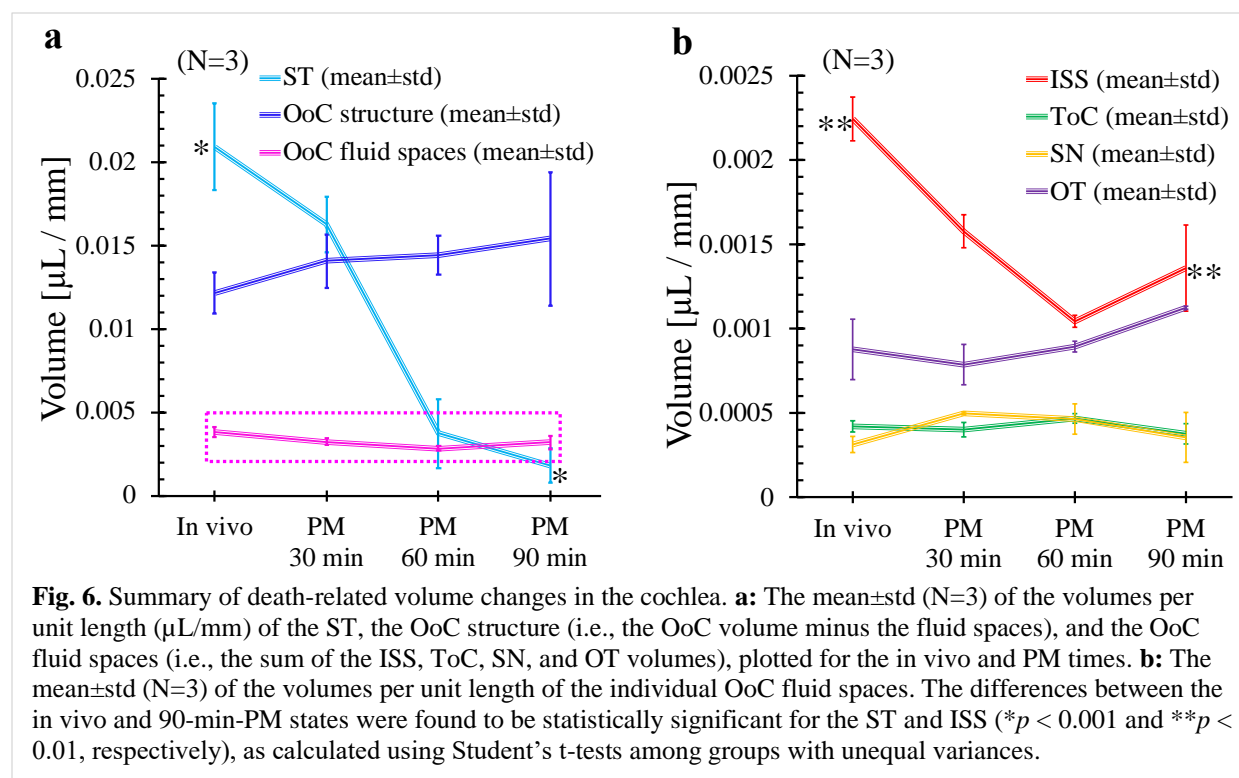157   Other OoC dimensions shown in Figure 4 include the ToC (b), SN (c), and OT (d). For the
158 ToC and SN, the PM changes relative to in vivo were minimal. A portion of the OT boundary is
159 formed by tectal cells (Fig. 1b, c), which can be mistaken as Hensen's cells (Henson et al., 1983).
160 Tectal cells are morphologically distinct from Hensen's cells, because their membranes form part
161 of the OT fluid space and they are not in contact with the BM (Spicer and Schulte, 1994). The
162 outer wall of the OT is made up of tectal cells, the roof is formed by the tectal-cell extension (TCE),
163 and the medial boundary is formed by the third row of phalangeal processes (PhPs), OHCs, and
164 Deiters' cells (Fig. 1b, c). The 90-min PM OT dimensions (Fig. 4e-i–ii) generally increased
165 relative to the in vivo case for longitudinal positions apical to the 500-µm location.
166   The minor/major axis-length ratios indicate the degree to which the cross section of the fluid
167 space is circular (0.75–1.0), elliptical (0.5–0.75), or oblong (<0.5; Fig. 4, bottom row). In general,

9

168   the ISS (Fig. 4b-iii) was elliptical in cross section and did not change much from in vivo to 90-
169   min PM. The ToC (Fig. 4c-iii) and OT (Fig. 4e-iii) were generally circular for the in vivo case and
170   changed somewhat at 90-min PM. The SN (Fig. 4d-iii) was generally more oblong than the other
171   fluid spaces. Detailed knowledge of the shapes of the OoC fluid spaces will likely be important
172   considerations when constructing finite element (FE) models to better understand the structure–
173   function relationship of the OoC fluid spaces.

Fig. 5. Death-related changes to the ST and OoC fluid volumes. **a–b:** 3D reconstructions of the ST and OoC fluid spaces (ISS, ToC, SN, and OT) based on OCT scans of a representative ear (#269), taken in vivo (**a**), and 90 min after death (**b**). **c–g**: The volume per unit length (µL/mm) is plotted for the in vivo state and each PM time, for the ST (**c**), ISS (**d**; note the change in scale for the second row), ToC (**e**), SN (**f**), and OT (**g**). The mean±std error bars (N=3) are shown as solid-blue lines, and the results from individual ears are shown as colored dashed lines.

174
175   To better quantify the progression of PM changes over time, Figure 5 plots the OoC fluid-
176   space volumes for the in vivo state and three PM states 30 min apart. Figure 5a, b shows segmented
177   3D OCT volume images for a representative animal (#269) for the in vivo (Fig. 5a) and 90-min-
178   PM (Fig. 5b) states. The significant decrease in ST volume (purple) after death is readily apparent.
179   Figure 5c–g contains plots of the ST, ISS, ToC, SN, and OT volumes (normalized by the
180   longitudinal length of the segmented region) as time progresses, for three animals. The volumes
181   of both the ST (Fig. 5c) and ISS (Fig. 5d) decreased systematically from in vivo to 60-min PM.
182   The ISS volume recovered slightly by 90-min PM, whereas the ST volume continued to decrease.
183   The ToC and SN volumes did not change significantly (Fig. 5e, f). On the other hand, the OT
184   volume (Fig. 5g) increased slightly from in vivo to 90-min PM. Table SI-1 lists the corresponding
185   values. PM decreases in the ISS cross-sectional dimensions could be due in part to PM swelling
186   of the sulcus cells. However, this is likely to be a small effect. The decrease in cross-sectional
187   dimensions more likely suggests that the ISS experiences internal pressure in the living cochlea
188   and that this internal pressure decreases during and after death.
189
190
191

10

Fig. 6. Summary of death-related volume changes in the cochlea. **a:** The mean±std (N=3) of the volumes per unit length (µL/mm) of the ST, the OoC structure (i.e., the OoC volume minus the fluid spaces), and the OoC fluid spaces (i.e., the sum of the ISS, ToC, SN, and OT volumes), plotted for the in vivo and PM times. **b:** The mean±std (N=3) of the volumes per unit length of the individual OoC fluid spaces. The differences between the in vivo and 90-min-PM states were found to be statistically significant for the ST and ISS (*$p < 0.001$ and **$p < 0.01$, respectively), as calculated using Student's t-tests among groups with unequal variances.

Comparing the structure and fluid-space volumes of the OoC

Figure 6a summarizes the progression of changes in OoC structure and fluid-space volumes from in vivo to 90-min PM. Figure 6a shows that (1) from in vivo to 90-min PM, the average ST volume decreased by more than a factor of 10; (2) the OoC structure alone (without fluid spaces) increased in volume by 25%; and (3) the OoC fluid spaces (all added together) decreased slightly in volume by 20%.

Figure 6b summarizes the volume changes of the individual OoC fluid spaces (the ISS, ToC, SN, and OT). Among these, the ISS changed the most after death, decreasing by about 50% from in vivo to 60-min PM (red line). By 90-min PM, the ISS volume had increased slightly. The OT volume (purple line) increased by 20% from in vivo to 90-min PM. Very little change was observed in the smaller ToC (green line) and SN (yellow line) volumes.

The in vivo fluid volumes were statistically compared to each of the PM states using a two-sided Student's t-test with unequal variances. Only the differences between the in vivo and 90-min-PM volumes of the ST (*; $p < 0.001$) and ISS (**; $p < 0.01$) were statistically significant. The lack of significant changes in the other variables may be due to the small number of animals used.

Some of the PM changes might have resulted from a change in cochlear temperature, which we did not monitor. The animals were placed on a heating pad throughout the measurements, and thus the core body temperature was maintained (See SI-1 for detail).

OCT vs. histology comparisons

In histological preparations of the cochlea, distortions of the cochlear tissue can arise in multiple ways. In Figures 3–6, we demonstrated and quantified the distortions to the in vivo OoC morphology that take place due to death alone. Additional well-known factors that can distort the OoC structure and fluid spaces include tissue fixation, decalcification, dehydration, embedding,

218 and staining procedures required for histological tissue preparation (Merchant, 2010). To
219 quantitatively assess the degree of combined OoC distortions due to death and histological
220 processing, the OoC morphology was measured after processing with histological methods (N=4).
221

Fig. 7. Comparisons of cochlear measurements between OCT (in vivo and PM) and histology (PM only). **a:** An in vivo OCT image shows a cross section of the gerbil OoC ~ 570 µm from basal end of the cochlea. Animal #274. **b:** An image of a histological OoC cross section (#274L-166) from the same ear as in **a**, at a comparable location (about 560 µm from basal end). **c:** An enlarged view of the black box from **b**, showing key OoC structures and the OT (dashed oval; note that the scale bars in **b** and **c** are different). **d:** Cochlear volumes obtained from a µCT scan (gray) and histology (magenta), from two different animals, overlap indicating little change in bony structures due to histology. **e–f:** The volumes per unit length (µL/mm) of the ST fluid space (**e**) and OoC structure (*including* the OoC fluid spaces in this case; **f**) are compared between OCT and histology methods. The OCT results are plotted for the in vivo and PM states in terms of the mean±std (N=3; blue lines), and for the in vivo state of an individual ear (#274; magenta diamonds). The histology results at a comparable location in the same animal (#274, magenta triangles) and as the mean±std (N=4, green diamonds) are plotted to the right. **g–h:** The measured width (OoC_W; **g**) and height (OoC_H; **h**) of the OoC structure are plotted as functions of longitudinal position. The OCT results are plotted for the in vivo mean±std (N=5; blue lines). Note that the gray diamonds correspond to the in vivo OCT and histology measurements of panels **a** and **b-c** respectively. For the OCT method, both the mean±std (blue lines) and individual ear (#274L; thin magenta lines) results are for the in vivo state. The histology measurements are plotted for an individual ear (#274L; thick magenta lines) alongside the mean±std (N=4; green lines).
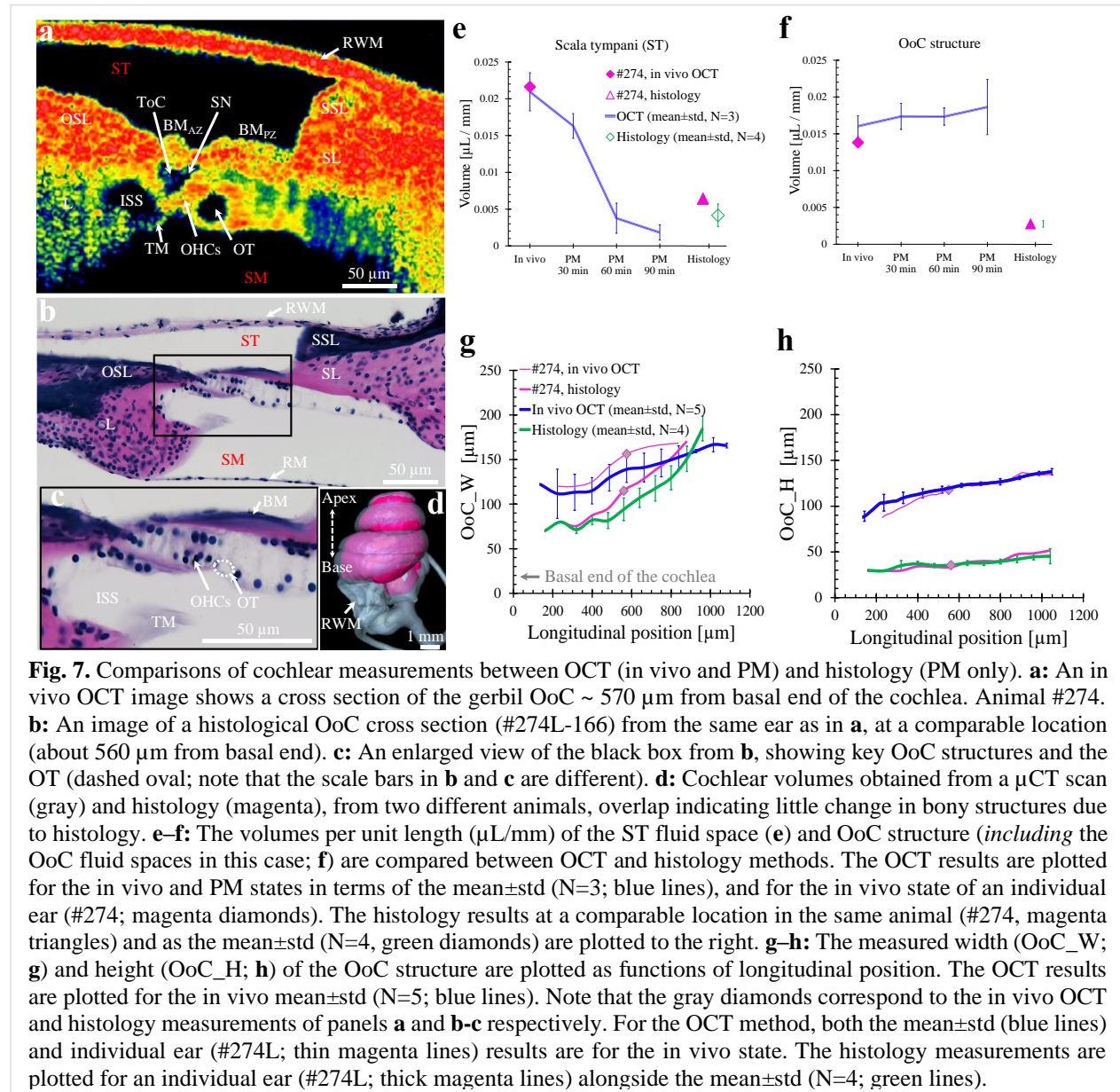
222
223 Figure 7 contrasts two cross-sectional images of the hook region in the same gerbil cochlea
224 (#274): the first was taken in vivo using OCT (Fig. 7a) and the second was obtained through
225 histological methods at approximately the same location (Fig. 7b). The differences between the
226 two images are striking. In Figure 7b (enlarged in Fig. 7c), the TM appears detached, which is
227 sometimes the case with histology, whereas it appears to be normally attached (but less visible) in
228 the in vivo OCT image. In the histological preparation, not only are the SN and ToC fluid spaces
229 hard to distinguish from the OoC structures, but also the OT volume space is dramatically reduced
230 (white dotted circle in Fig. 7c; note the scale bars are different), and the dimensions of the OoC

12

231   structures appear significantly smaller than those of the in vivo OCT image, especially the OoC_H
232   dimension. In addition, the BMAZ and BMPZ regions are distinguishable in the in vivo OCT
233   image, but a clear boundary between these regions is not visible in the histological image. To
234   verify the dimensions from the histology method, the cochlear volumes from two different animals
235   were segmented, reconstructed, and the outer surfaces aligned (Fig. 7d) based on both a µCT scan
236   (gray) and the histology slices (magenta). The resulting bony volumes overlap, which provides a
237   means of checking that the gross dimensions of the bony structures have not changed and changes
238   observed in the OoC dimensions with histology are due to shrinking of the OoC.
239   The OoC dimensions measured with OCT can be compared against those measured by
240   histology. Figure 7e shows the mean±std volume/mm of the ST in multiple animals (N=4)
241   processed with histology (green diamond with error bars), and from an individual ear measured
242   using both OCT and histology (#274; magenta diamond and triangle, respectively). These
243   measurements are compared against the sequence of OCT measurements from in vivo to 90-min
244   PM from Figure 6a (N=3; blue line and error bars). The histology-based ST volume for the
245   individual animal (magenta triangle) was about 50% greater than the mean histology-based volume
246   across ears (green diamond). However, the in vivo OCT-based volume on the same individual ear
247   (magenta diamond) was about three times greater than the histology-based volume. The histology-
248   based volume was comparable to the average of the 60- and 90-min PM volumes (Table SI-2
249   reports values). Figure 7e shows that a significant amount of the change in ST volume took place
250   between 30- and 60-min PM. For histological processing, the animal is perfused in vivo with a
251   fixative that takes effect within 5 min. In the absence of this perfusion step, however, there was
252   little change in the ST volume during the first 30 min after death (Fig. 7e, blue line). Thus, most
253   of the shrinkage present in the ST volumes in the histological samples likely occurred during this
254   chemical-perfusion stage of histological processing.
255   Figure 7f compares the volumes (per mm) of the OoC structure (now *including* the OoC fluid
256   spaces) as measured using OCT and histology. The OCT results from in vivo to 90-min PM (N=5;
257   mean±std, blue line) and for one in vivo ear (magenta diamond) are shown alongside the mean±std
258   histology results (N=4, green diamond with error bars concealed by the symbol) and the individual
259   histology results from the same individual in vivo ear (magenta triangle). As mentioned above, the
260   OoC fluid spaces were hard to discern using the histological method, so no attempt was made to
261   subtract those out. The mean volume of the OoC structure (with included fluid spaces) as measured
262   in vivo with OCT (blue line) was about 4.9 times greater than that measured with histology (green
263   diamond), and for the individual ear (magenta diamond vs. triangle) this ratio was about 4.7 times.
264   The volume of the OoC structure was found by integrating the measured cross-sectional areas.
265   These areas were also similarly greater when measured in vivo than when measured with histology
266   (Fig. SI-5a).
267   Figure 7g and h compare OoC_W and OoC_H, respectively, as measured in vivo vs. in the
268   histological material. Going from the basal end towards the apex, the histology based average
269   OoC_W increases rapidly (Fig. 7g, green line and error bars; N=4). The OCT-based in vivo
270   OoC_W values (Fig. 7g, blue line and error bars; N=5) have a shallower slope than histology and
271   are about 2 times larger than the corresponding histology values at the basal end (near 0.1 mm),
272   but slightly smaller at the more-apical end (near 0.9 mm). Furthermore, the OCT-based in vivo
273   OoC_H values (Fig. 7h) are about 2–3 times larger than those from the corresponding histology
274   measurements. For the individual ear, the differences between the OCT- and histology-based
275   widths (Fig. 7g; thin and thick magenta lines, respectively) appear slightly greater than those
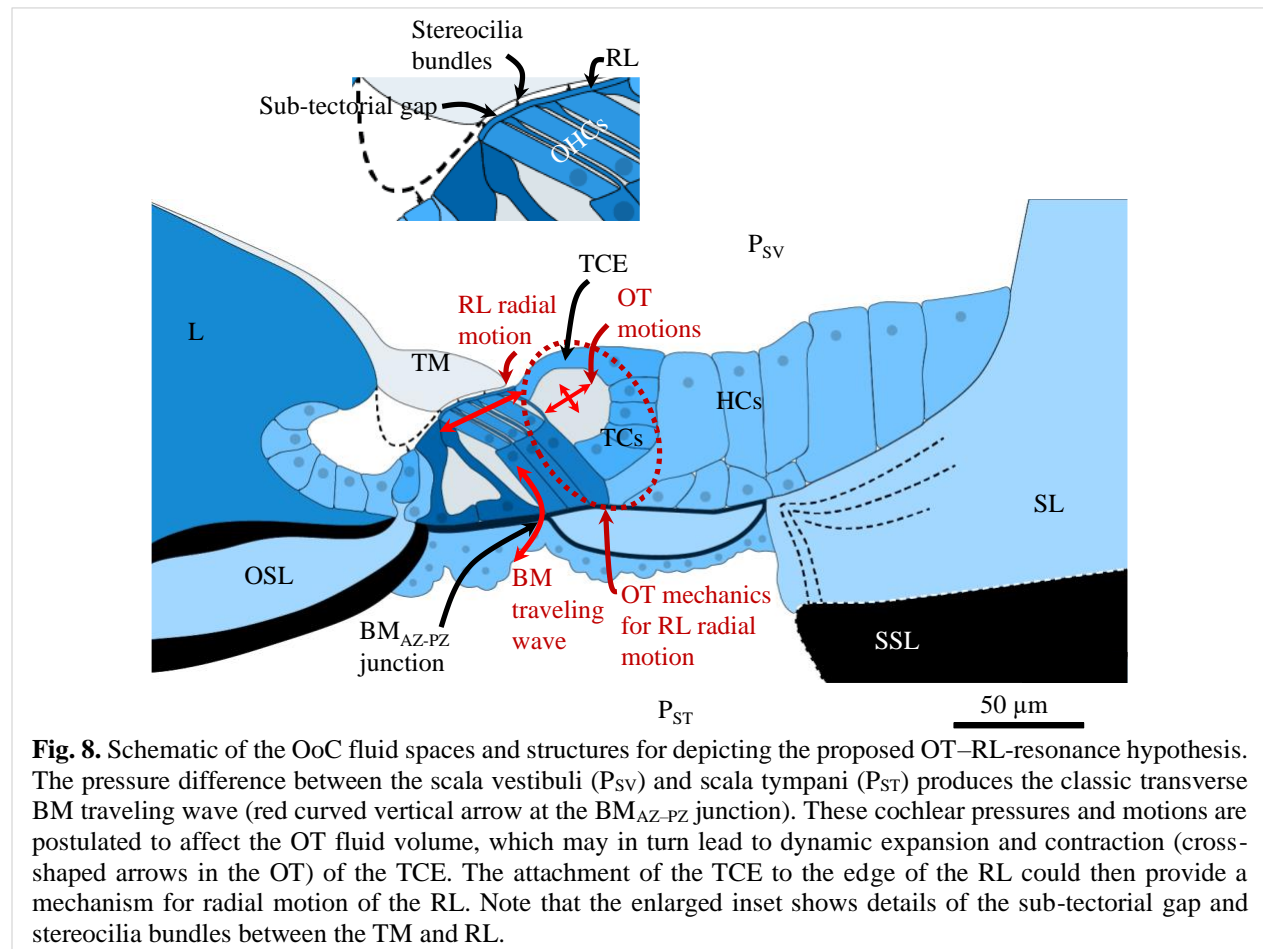276   between the average widths but also with a steeper slope for histology. The histology-based

277   volume (per mm) and dimensions of the OoC structure are smaller in comparison to the in vivo
278   case (Fig. 7), and the in vivo case is typically smaller than the PM cases (Fig. 3e,f). Recall that for
279   histology, the fixative was in vivo with cardiac perfusion. From this we surmise that the decrease
280   in dimensions in histology (Fig. 7, Fig. SI-5) are not due to PM effects (Fig. 3e,f), but rather due
281   to histological processing. The one caveat is the tangential sectioning angle that in histology could
282   affect the width dimensions, which explains the steeper slope in their width measurements. But
283   the tangential sectioning angle would not affect the height. However, the height with histology
284   decreases quite a bit (Fig. 7g) which again argues that processing decreased the OoC dimensions.
285   The reasons for the smaller width in the basal end are not clear, but this implies that the ridges
286   used to define the OoC_W have moved closer toward each other during histological processing.
287

III. Discussion

289   Our OCT measurements show that anatomical changes take place in the gerbil high-frequency
290   cochlear hook region shortly after death. Some of these changes become apparent within 30-min
291   PM, while others manifest later, e.g., at 90-min PM. Although the advantages of high in-plane
292   resolution as achieved by staining with histology are undeniable, the present OCT-based results
293   demonstrate that our histology-based understanding of the in vivo OoC anatomy has been highly
294   distorted, in the high-frequency hook region. Some of these distortions are due to PM effects, while
295   others are due to histological processing. OCT provides a far more accurate view of in vivo
296   cochlear anatomy and PM effects than has been possible before. The tube-like OT, at the outer
297   border of the RL, and the ISS changed the most from in vivo to 90-min PM. These OCT
298   observations lead us to speculate about the roles of the OT and ISS in OoC mechanics and sound
299   transduction.
300   A pressure difference across the OoC results in a classic traveling wave and transverse motion
301   of the BM (Fig. 8, red curved vertical arrow), which in gerbils reaches a peak at the BM_{AZ-PZ}
302   junction (Cooper et al., 2018). This OoC motion produces pulsatile motion of the cell walls
303   surrounding the OT fluid space (Fig. 8). Depending on the wall stiffness, fluid mass, and steady-
304   streaming Reynolds number, the wall motion may excite resonance modes (Secomb, 1978). We
305   hypothesize that OT resonance modes can induce radial and transverse motions of the TCE, which
306   is attached to the outer edge of the RL and thus provides a mechanism for radial motion of the RL
307   (Fig. 8, red dotted ellipse). Could motion of the OT extracellular fluid space result in a radial RL
308   motion whose phase is important for cochlear amplification? It is generally established that the
309   motion difference between the RL and TM, which causes the OHC stereocilia to deflect, needs to
310   occur with a particular phase relationship to the BM motion so that OHC somatic motility pushes
311   the BM in the direction of BM velocity, such that this motion then opposes viscous losses and
312   results in cochlear amplification (Gummer et al., 1996; Sasmal et al., 2020; Wang et al., 2016).
313   Achieving the correct phase relationship has been attributed to a TM resonance that causes a lag
314   in the radial phase of the TM, starting at about ½-octave below the best frequency (Gummer et al.,
315   1996; Lukashkin et al., 2010; Sasmal and Grosh, 2019). However, recent OCT-based vibrometry
316   measurements have challenged this view, and the TM-resonance hypothesis has been rejected in
317   favor of an alternative hypothesis positing that the source of this special phase relationship is
318   instead a lead in the radial phase of the RL (Guinan, 2020). This hypothesis that the RL provides
319   a leading phase is consistent with the above-best-frequency resonances observed in mouse radial
320   RL and TM motions (Lee et al., 2016). Additional support comes from measurements near the OT
321   in an area called the "lateral compartment", which show significant in vivo and PM radial motion

322   with the correct phase for triggering OHC somatic motility in the required manner to amplify OoC
323   motion.
324

Fig. 8. Schematic of the OoC fluid spaces and structures for depicting the proposed OT–RL-resonance hypothesis. The pressure difference between the scala vestibuli (P_{SV}) and scala tympani (P_{ST}) produces the classic transverse BM traveling wave (red curved vertical arrow at the BM_{AZ-PZ} junction). These cochlear pressures and motions are postulated to affect the OT fluid volume, which may in turn lead to dynamic expansion and contraction (cross-shaped arrows in the OT) of the TCE. The attachment of the TCE to the edge of the RL could then provide a mechanism for radial motion of the RL. Note that the enlarged inset shows details of the sub-tectorial gap and stereocilia bundles between the TM and RL.

325

326   However, to our knowledge no mechanism has yet been published that could explain how such
327   a shift in the RL phase could arise. We postulate that the mass of the OT fluid volume, coupled
328   with the stiffness of its surrounding cells, could form an OT–RL resonant structure capable of
329   supporting resonant modes with phase leads in the best-frequency region. This OT–RL resonance
330   would be present for passive mechanics and is hypothesized to be amplified by the active pumping
331   of fluid into the OT by the OHCs.
332   The ToC, SN, and OT fluid spaces all contain the same cortilymph fluid (gray color, Fig. 8),
333   and have interstitial fluid communication through the spaces around the OHCs and the spaces
334   between the OPCs. It has been observed that electrical excitation of OHC motility causes a
335   pumping of fluid through the SN and into the ToC, and that this possibly enhances cochlear
336   amplification through yet-to-be discovered mechanisms (Karavitaki and Mountain, 2007). A
337   recent FE modeling study features a representation of the gerbil mid-frequency OoC interstitial
338   fluid spaces, and suggests that the role of the interconnected OoC fluid spaces is to redistribute
339   pressure from OHC contractions so as to avoid excessive pressure buildup in the cortilymph space
340   (Zagadou et al., 2020). Comparable FE studies of the high-frequency hook region are currently
341   lacking. Our anatomical measurements will facilitate the building of such models to test the OT–
342   RL-resonance hypothesis presented here.

343 Does the OT fluid space play a role in longitudinal coupling in the OoC? The OHC-fluid-
344 pumping hypothesis (Karavitaki and Mountain, 2007) predicts the flow of cortilymph through the
345 SN and into the ToC, which would then cause the propagation of a longitudinal wave within the
346 ToC. This fluid wave could interact with the classic BM traveling wave and provide a mechanism
347 for longitudinal coupling between neighboring sections of the OoC (Karavitaki and Mountain,
348 2007; Zagadou and Mountain, 2012). Thus, using a similar argument as for the ToC, the OT fluid
349 space may also act to promote longitudinal coupling in the OoC. This form of longitudinal coupling
350 would act in addition to other known mechanisms of longitudinal coupling, such as that between
351 neighboring radial collagen fibers of the BM (Von Békésy, 1960), and that caused by the
352 viscoelastic material properties of the TM (Ghaffari et al., 2007; Meaud and Grosh, 2010).
353 Longitudinal coupling in the OoC is also provided by the Y-shaped building blocks that form part
354 of the structure between the RL and BM (each consisting of a Deiters' cell extending out from the
355 BM, with its PhP and an attached OHC branching out at different angles to join the RL), which
356 are thought to be key for OoC amplification (Motallebzadeh et al., 2018). The relative importance
357 of longitudinal coupling due to wave propagation in the OoC fluid spaces, vs. that due to the
358 motions of structural components of the OoC, has yet to be determined. Such quantitative
359 determinations are likely best approached using computational-modeling efforts.
360 The OT may also play a role in ion transport, given that the tectal cells of the OT feature
361 fimbriae suggestive of cells active in ion resorption (Spicer and Schulte, 1994). There is K+
362 transport from the base of the OHCs to the Deiters' cells, and then diffusion via gap junctions
363 between the Deiters' cells, Hensen's cells and Claudius cells, back toward the stria vascularis
364 (Kikuchi et al., 2000). It has been proposed that sound-induced K^+-ion efflux from the OHCs flows
365 into the OT through the interstitial cortilymph fluid (Spicer et al., 2003). These ions would then be
366 absorbed and also channeled through parallel pathways of tectal cells, the third row of Deiters'
367 cells, and Hensen's cells, and ultimately find their way toward the stria vascularis (Spicer et al.,
368 2003). The one caveat here is that tectal cells were only seen in the mid to upper turns and not the
369 basal high frequency region (Spicer et al., 2003). However, this result was based on histology
370 studies which distorts the OoC in that region (Fig. 7). Thus, the OT might play a dual role in both
371 OoC mechanics and ion transport.
372 The decrease in the ISS cross-sectional volume due to the in vivo–PM transition (Figs. 4a, 6b)
373 may have functional significance for IHC and OHC transduction. It is likely that the PM decrease
374 in ISS volume indicates an in vivo regulation of the static pressure within the ISS. Such an in vivo
375 pressure would also maintain a height gap between the TM and RL (Fig. 8, inset image). Because
376 the stiffness of the TM is much less than that of the OHC stereocilia bundles, a sub-tectorial static
377 pressure would be expected to push on the TM to maintain an optimal position just above the top
378 of the tallest row of IHC and OHC stereocilia bundles embedded in the TM. A decrease in ISS
379 static pressure due to death could decrease the sub-tectorial pressure, which would then likely
380 decrease the gap opening and gap height, and thereby possibly disrupt the normal IHC and possibly
381 OHC transduction processes. A change in gap height might also change the angulation of the OHC
382 stereocilia bundles, and thus the bias point for mechano-electric transduction.
383 Regulation of the sub-tectorial gap opening and gap height due to the pressure in the ISS could
384 be controlled by the aquaporins found in the inner-sulcus cells, which could control the flow of
385 water molecules to and from the ISS (Beitz et al., 2003; Eckhard et al., 2014; Stankovic et al.,
386 1995). Another possible mechanism for pressure regulation is through voltage-regulated ion
387 channels. We postulate that ISS pressurization is necessary to maintain the gap opening near the
388 IHC and the adjoining sub-tectorial gap height between the TM and RL in the living cochlea, and

389 that the loss of this pressurization after death is a contributing factor to the PM loss of cochlear
390 function that has not been previously considered.
391   From these OCT-based observations, we have postulated a new OT–RL-resonance theory, and
392 a new mechanism by which ISS pressurization regulates the sub-tectorial gap opening and gap
393 height. Testing these hypotheses will require new physiological measurements accompanied by
394 steadily improving OCT methods, as well as further developments in FE modeling approaches.
395

IV. Materials and Methods

396

Animals and surgical approach

397
398   This study was approved by the Institutional Animal Care and Use Committee (IACUC) at
399 Massachusetts Eye and Ear (MEE). Healthy Mongolian gerbils (N=14, aged 5–32 weeks, weight
400 range 60–111 g) of either sex (7 males, 7 females) were used for this study. Results are reported
401 from the five left ears for the OCT and both ears of two animals for histology volume scans were
402 obtained. The surgical procedures and equipment setup are reported in SI-1.
403

OCT system and volume scans

404
405   All OCT imaging measurements were made using a Spectral Domain–OCT (SD-OCT) system
406 with a 905-nm center wavelength and a 100-kHz high-speed line-scan camera (GAN620C1,
407 Thorlabs, Germany). The system was operated using custom LabVIEW-based software (VibOCT
408 version 1.6). Camera images of the anatomical approach were obtained and used to determine and
409 record the region of interest for the OCT scans (e.g., the black dotted square box in Fig. 1a).
410 VibOCT provides real-time depth-resolved 1D A-scan, 2D cross-sectional B-scan, and 3D
411 volumetric C-scan imaging. The axial resolution was ~1.4 µm (in water, with a refractive index
412 of 1.33), and the lateral resolution was ~1.95 µm, using a 30.5-mm, 0.26-NA long-working-
413 distance, 10× objective lens (M Plan Apo NIR, Mitutoyo, Aurora, IL, USA). To minimize
414 variations among the 3D-volume OCT scans across animals, the orientation of the gerbil head in
415 the head holder, as well as settings on the positioning stage and goniometer, were kept similar
416 across experiments.
417   While the penetration depth of the OCT system is approximately 1.44 mm (in water), the best
418 B-scan image quality was obtained for depths of less than 300 µm. Because the effective depth of
419 field is smaller than the depth range of interest of about 1-1.2 mm, three or more 3D volume scans
420 were acquired at different focal depths, and tracked by the fine focus adjustment on the OCT
421 optical head with ~1-µm resolution using a Vernier scale (Cho et al., 2018). A single 3D volumetric
422 C-scan consisted of a longitudinal stack of 512 B-scans that are each 1,024 (A-line depth) × 512
423 (radial), with each C-scan volume averaged 10 times.
424   All sub-volume scans (each covering a different depth range) were concatenated using ImageJ
425 software to obtain a complete volume stack. The non-overlapping portions from each depth range
426 were extracted, and these portions were then concatenated to obtain a full volume of the OoC in
427 the basal end of the cochlea (the hook region), including the RWM and RM.
428   All OoC-structure and fluid-space volumes were segmented from the 3D-volume OCT
429 measurements. More details on the 3D-reconstruction and segmentation methods are provided in
430 Figs. SI-2 and 3 for the OoC structure, and in Fig. SI-4 for the OoC fluid spaces.
431
432
433

Histological preparations

After completing the in vivo 2D and 3D OCT morphological measurements, the anatomies of three gerbils (#192, #274, and #338) were additionally quantified using histological methods, consisting of tissue fixation (using a 4% formaldehyde, 1% acetic acid, 0.1% glutaraldehyde solution) followed by celloidin embedding (O'Malley et al., 2009). Each animal was first intracardially perfused, and then its whole head was extracted, decalcified, and H&E stained, all of which was performed by the Otopathology Laboratory at MEE. Serial sections of the whole skull, including both individual ears, were cut (along the sagittal plane) into 20-µm-thick slices, with every other slice stained to create histology slides. Thus, the histology sections were spaced at 40-µm intervals. The slides were digitized and then reconstructed and segmented into 3D volume stacks for direct comparison against the OoC morphology as obtained using OCT methods (see SI-6 for details).

Acknowledgements

Author contributions

N.H.C. and S.P conceived of and designed the project. N.H.C developed the VibOCT software, conducted the experiments, and reconstructed the 3D OCT volumes. H.W performed the segmentation and analysis of the 3D volumes from OCT and histology. S.P, N.H.C, and H.W. wrote and edited the manuscript, and S.P. supervised the project.

Data availability

All data needed to evaluate the conclusions in the paper are present in the paper. Additional data related to this paper may be requested from the authors.

Conflicts of interest

All the authors declare that they have no conflicts of interest.

Supplementary information is available for this paper.

References

Agrawal S, Schart-Morén N, Liu W, Ladak HM, Rask-Andersen H, Li H. 2018. The secondary spiral lamina and its relevance in cochlear implant surgery. *Ups J Med Sci* **123**:9–18. doi:10.1080/03009734.2018.1443983

Beitz E, Zenner H-P, Schultz JE. 2003. Aquaporin-Mediated Fluid Regulation in the Inner Ear. *Cell Mol Neurobiol* **23**:315–329. doi:10.1023/A:1023636620721

Cho NH, Guan X, Ravicz ME, Puria S. 2018. Human tympanic membrane shape and thickness distribution measured with optical coherence tomography (OCT). Presented at the Asso. Res. Otolaryngology. San Diego, CA, US.

Cho NH, Lee JW, Cho J, Kim J, Jang JH, Jung W. 2015. Evaluation of the usefulness of three-dimensional optical coherence tomography in a guinea pig model of endolymphatic hydrops induced by surgical obliteration of the endolymphatic duct. *Journal of biomedical optics* **20**:036009.

Cooper NP, Vavakou A, van der Heijden M. 2018. Vibration hotspots reveal longitudinal funneling of sound-evoked motion in the mammalian cochlea. *Nat Commun* **9**:3054. doi:10.1038/s41467-018-05483-z

Eckhard A, Müller M, Salt A, Smolders J, Rask-Andersen H, Löwenheim H. 2014. Water permeability of the mammalian cochlea: functional features of an aquaporin-facilitated water shunt at the perilymph–endolymph barrier. *Pflugers Arch - Eur J Physiol* **466**:1963–1985. doi:10.1007/s00424-013-1421-y

Edge RM, Evans BN, Pearce M, Richter C-P, Hu X, Dallos P. 1998. Morphology of the unfixed cochlea. *Hearing research* **124**:1–16.

Ghaffari R, Aranyosi AJ, Freeman DM. 2007. Longitudinally propagating traveling waves of the mammalian tectorial membrane. *Proc Natl Acad Sci U S A* **104**:16510–16515. doi:10.1073/pnas.0703665104

Guinan JJ. 2020. The interplay of organ-of-Corti vibrational modes, not tectorial- membrane resonance, sets outer-hair-cell stereocilia phase to produce cochlear amplification. *Hearing Research* **395**:108040. doi:10.1016/j.heares.2020.108040

Gummer AW, Hemmert W, Zenner HP. 1996. Resonant tectorial membrane motion in the inner ear: its crucial role in frequency tuning. *Proceedings of the National Academy of Sciences* **93**:8727–8732. doi:10.1073/pnas.93.16.8727

Hardie NA, MacDonald G, Rubel EW. 2004. A new method for imaging and 3D reconstruction of mammalian cochlea by fluorescent confocal microscopy. *Brain Research* **1000**:200–210. doi:10.1016/j.brainres.2003.10.071

Henson MM, Jenkins DB, Henson OW. 1983. Sustentacular cells of the organ of Corti — the tectal cells of the outer tunnel. *Hearing Research* **10**:153–166. doi:10.1016/0378-5955(83)90051-5

Hu X, Evans BN, Dallos P. 1999. Direct visualization of organ of Corti kinematics in a hemicochlea. *Journal of neurophysiology* **82**:2798–2807.

Huang D, Swanson EA, Lin CP, Schuman JS, Stinson WG, Chang W, Hee MR, Flotte T, Gregory K, Puliafito CA. 1991. Optical coherence tomography. *science* **254**:1178–1181.

Iyer JS, Batts SA, Chu KK, Sahin MI, Leung HM, Tearney GJ, Stankovic KM. 2016. Micro-optical coherence tomography of the mammalian cochlea. *Sci Rep* **6**:33288. doi:10.1038/srep33288

Kapuria S, Steele CR, Puria S. 2017. Unraveling the mystery of hearing in gerbil and other rodents with an arch-beam model of the basilar membrane. *Scientific Reports* **7**:228. doi:10.1038/s41598-017-00114-x

Karavitaki KD, Mountain DC. 2007. Evidence for outer hair cell driven oscillatory fluid flow in the tunnel of Corti. *Biophysical journal* **92**:3284–3293.

Kikuchi T, Adams JC, Miyabe Y, So E, Kobayashi T. 2000. Potassium ion recycling pathway via gap junction systems in the mammalian cochlea and its interruption in hereditary nonsyndromic deafness. *Medical Electron Microscopy* **33**:51–56. doi:10.1007/s007950070001

Kim J, Xia A, Grillet N, Applegate BE, Oghalai JS. 2018. Osmotic stabilization prevents cochlear synaptopathy after blast trauma. *Proceedings of the National Academy of Sciences* **115**:E4853–E4860.

Lee HY, Raphael PD, Xia A, Kim J, Grillet N, Applegate BE, Ellerbee Bowden AK, Oghalai JS. 2016. Two-Dimensional Cochlear Micromechanics Measured In Vivo Demonstrate Radial Tuning within the Mouse Organ of Corti. *Journal of Neuroscience* **36**:8160–8173. doi:10.1523/JNEUROSCI.1157-16.2016

Lim DJ, Anniko M. 1985. Developmental Morphology of the Mouse Inner Ear: A scanning electron microscopic observation. *Acta Oto-Laryngologica* **99**:5–69. doi:10.3109/00016488509121766

Liu GS, Kim J, Applegate BE, Oghalai JS. 2017. Computer-aided detection and quantification of endolymphatic hydrops within the mouse cochlea in vivo using optical coherence tomography. *Journal of Biomedical Optics* **22**:076002.

Lukashkin AN, Richardson GP, Russell IJ. 2010. Multiple roles for the tectorial membrane in the active cochlea. *Hearing Research* **266**:26–35. doi:10.1016/j.heares.2009.10.005

Meaud J, Grosh K. 2010. The effect of tectorial membrane and basilar membrane longitudinal coupling in cochlear mechanics. *J Acoust Soc Am* **127**:1411–1421. doi:10.1121/1.3290995

Meenderink SWF, Shera CA, Valero MD, Liberman MC, Abdala C. 2019. Morphological Immaturity of the Neonatal Organ of Corti and Associated Structures in Humans. *JARO* **20**:461–474. doi:10.1007/s10162-019-00734-2

Merchant SN. 2010. Schuknecht's Pathology of the Ear. PMPH-USA.

Motallebzadeh H, Soons JAM, Puria S. 2018. Cochlear amplification and tuning depend on the cellular arrangement within the organ of Corti. *Proc Natl Acad Sci USA* **115**:5762–5767. doi:10.1073/pnas.1720979115

O'Malley JT, Merchant SN, Burgess BJ, Jones DD, Adams JC. 2009. Effects of Fixative and Embedding Medium on Morphology and Immunostaining of the Cochlea. *Audiol Neurootol* **14**:78–87. doi:10.1159/000158536

Peterson LC, Bogert BP. 1950. Erratum: A Dynamical Theory of the Cochlea. *The Journal of the Acoustical Society of America* **22**:640–640. doi:10.1121/1.1906668

Plassmann W, Peetz W, Schmidt M. 1987. The Cochlea in Gerbilline Rodents. *BBE* **30**:82–102. doi:10.1159/000118639

Richter C-P, Edge R, He DZZ, Dallos P. 2000. Development of the Gerbil Inner Ear Observed in the Hemicochlea. *JARO* **1**:195–210. doi:10.1007/s101620010019

Sasmal A, Geib N, Popa B-I, Grosh K. 2020. Broadband nonreciprocal linear acoustics through a non-local active metamaterial. *New J Phys* **22**:063010. doi:10.1088/1367-2630/ab8aad

Sasmal A, Grosh K. 2019. Unified cochlear model for low- and high-frequency mammalian hearing. *Proc Natl Acad Sci USA* **116**:13983–13988. doi:10.1073/pnas.1900695116

Secomb TW. 1978. Flow in a channel with pulsating walls. *Journal of Fluid Mechanics* **88**:273–288. doi:10.1017/S0022112078002104

Souter M, Nevill G, Forge A. 1995. Postnatal development of membrane specialisations of gerbil outer hair cells. *Hearing research* **91**:43–62.

Spicer SS, Schulte BA. 1994. Ultrastructural differentiation of the first hensen cell in the gerbil cochlea as a distinct cell type. *The Anatomical Record* **240**:149–156. doi:https://doi.org/10.1002/ar.1092400202

Spicer SS, Smythe N, Schulte BA. 2003. Ultrastructure indicative of ion transport in tectal, Deiters, and tunnel cells: Differences between gerbil and chinchilla basal and apical cochlea. *Anat Rec* **271A**:342–359. doi:10.1002/ar.a.10041

Stankovic KM, Adams JC, Brown D. 1995. Immunolocalization of aquaporin CHIP in the guinea pig inner ear. *American Journal of Physiology-Cell Physiology* **269**:C1450–C1456. doi:10.1152/ajpcell.1995.269.6.C1450

Von Békésy G. 1960. Experiments in hearing., McGraw-Hill series in psychology. New York: McGraw.

Wang Y, Steele CR, Puria S. 2016. Cochlear Outer-Hair-Cell Power Generation and Viscous Fluid Loss. *Sci Rep* **6**:19475. doi:10.1038/srep19475

Zagadou BF, Barbone PE, Mountain DC. 2020. Significance of the Microfluidic Flow Inside the Organ of Corti. *Journal of Biomechanical Engineering* **142**:081009. doi:10.1115/1.4046637

Zagadou BF, Mountain DC. 2012. Analysis of the Cochlear Amplifier Fluid Pump Hypothesis. *JARO* **13**:185–197. doi:10.1007/s10162-011-0308-x